Journal of Materials Chemistry A

COMMUNICATION

View Article Online
View Journal | View Issue

Cite this: J. Mater. Chem. A, 2016, 4, 3210

Received 12th January 2016
Accepted 28th January 2016

DOI: 10.1039/c6ta00328a

www.rsc.org/MaterialsA

Guest–host modulation of multi-metallic (oxy) hydroxides for superb water oxidation†

Cheng Tang, Hao-Fan Wang, Han-Sen Wang, Fei Wei and Qiang Zhang*

Multi-metallic (oxy)hydroxide materials are some of the most promising alternatives for superb water oxidation electrocatalysts. Herein, a series of graphene/NiFe (oxy)hydroxides were fabricated to investigate the role of the Fe/Ni ratio in regard to the resultant physical structures, decoration styles, and combined catalytic activities. With the Fe content increasing, a phase evolution from Fe doped $Ni(OH)_2$/NiO(OH) to Ni doped FeO(OH) was demonstrated. The moderate guest-metal substitution into the host-oxyhydroxide framework (Fe into Ni or Ni into Fe) substantially enhanced the oxygen evolution activity with a decrease in both the Tafel slope and overpotential. In addition, the NiO(OH) and FeO(OH) frameworks exhibited distinct properties and performances for the oxygen evolution reaction due to the different metal–oxygen bond lengths and adsorption energies of the intermediates.

The looming fossil energy crisis and urgent need for CO_2 emission reduction have stimulated intense attention and research for sustainable energy systems and next-generation energy storage technologies over past decades.[1] Recently, energy conversion and storage based on the hydrogen cycle rather than the carbon cycle has emerged rapidly and has been demonstrated to be a promising alternative, including H_2 generation from water splitting using electricity or sunlight and transformations between electrical/solar and chemical energy.[2–7] The oxygen evolution reaction (OER) ($4OH^- \rightarrow 2H_2O + O_2 + 4e^-$, in base) occupies the core status of the water splitting process; nevertheless, it is a kinetically sluggish half-reaction due to the four proton-coupled electron transfers and oxygen–oxygen bond formation. So far, noble metal oxides such as IrO_2 and RuO_2 are acknowledged as the state-of-the-art electrocatalysts for the OER, especially in acid, but they suffer greatly from their high cost as scarce resources.[8] Therefore, it is emergent to explore highly active, earth-abundant, and chemically stable catalysts to expedite this process and boost the reaction rate towards practical application.

Recently, transition-metal-based materials (Ni, Fe, Co, Mn, *etc.*) and their (oxy)hydroxides have been investigated extensively and have turned out to be excellent alternatives for OER catalysis, for example NiFe, NiFeAl, NiCo, CoFe, ZnCo, CoMn (oxy)hydroxides, *etc.*,[5,9–24] and particularly NiFe (oxy)hydroxides.[14,16,18,23–26] It's notable that among all of the reports, the multi-metallic (oxy)hydroxides are demonstrated to greatly surpass their monometallic counterparts, which has motivated systematic investigation of multi-metallic catalytic systems in terms of their chemical composition, physical structure, and hierarchical morphologies to ascertain the structure–property relationships and underlying catalytic mechanism.[12,14,27–29] Firstly, the partial substitution of the host (oxy)hydroxide framework is suggested to increase the electrical conductivity[30] and generate a layered double hydroxide (LDH) structure with enhanced electron transfer and mass intercalation.[16,31] In addition, a partial-charge-transfer activation effect is hypothesized from the doped metal cations,[16,32] which alters the electronic structure and oxidation states of adjacent host metal cations and the oxyhydroxide framework towards an increased activity.[12,31,33,34] In some other cases, the host (oxy)hydroxides are considered as a conductive and stable substrate[35] while the incorporated metal cations serve as the real active sites with a contractive metal–oxygen bond and edge-sharing octahedra.[29,36,37] In spite of studying all of these processes both experimentally and theoretically, there is still controversy about the actual active sites and the detailed mechanism, and thereby ambiguous instructions on the design and development of optimal multi-metallic catalysts for OER.[6]

The mechanistic investigation and elucidation is challenged by overcoming the poor conductivity, fully accessing the preconceived active sites, and the effective regulation of both the chemical composition and the crystal phases.[31] To address these issues, herein, we developed a series of novel graphene/NiFe (oxy)

Beijing Key Laboratory of Green Chemical Reaction Engineering, Department of Chemical Engineering, Tsinghua University, Beijing 100084, PR China. E-mail: zhang-qiang@mails.tsinghua.edu.cn

† Electronic supplementary information (ESI) available: Details of experimental details, XPS spectra, TGA curves, HRTEM images, FT-IR spectra, stability characterization, and model structures. See DOI: 10.1039/c6ta00328a

hydroxides (G/NiFe) for the study of the different roles of Ni/Fe, the optimized structure and underlying activity origins of multi-metallic (oxy)hydroxides involved in OER catalysis (Scheme 1a). Nanosized NiFe (oxy)hydroxides were uniformly located in the conductive graphene framework. A phase evolution from Fe doped $Ni(OH)_2$/NiO(OH) to Ni doped FeO(OH) with increased Fe addition is demonstrated for the first time, and the relationship between the composition and properties is elucidated in depth (Scheme 1b and c).

The mesoporous graphene framework was firstly fabricated through a MgO-templated chemical vapor deposition (CVD) method and then moderately oxidized to serve as the substrate. NiFe (oxy)hydroxides were generated on the graphene substrate *via* a typical urea-assisted co-precipitation with different molar ratios of the Ni/Fe precursors (4 : 0, 3 : 1, 1 : 3, 0 : 4). The resultant samples are denoted as G/$NiFe_x$ (0, 0.30, 0.56, 1.00), where x is the molar ratio of Fe/(Fe + Ni) as determined by X-ray photoelectron spectroscopy (XPS) (Fig. S1, Table S1†). For x = 0 and 1.00, the symbols are simplified as G/Ni and G/Fe. Taking G/$NiFe_{0.30}$ as example, the as-fabricated composite exhibits a pizza-like structure, with the mesoporous graphene and nanosized hydroxides decorated onto the scaffolds, as indicated in scanning electron microscopy (SEM) and transmission electron microscopy (TEM) images (Fig. 1a–c). Notably, the $NiFe_{0.30}$ hydroxides exhibit quite a uniform distribution, with an ultra-thin and nanosized appearance of typically *ca.* 5 nm, which is attributed to the interfacial anchor and spatial confinement from the mesoporous graphene substrate. Such a fabrication method leads to a composite with fully-accessible active sites of NiFe hydroxides and enhanced electrical conductivity from graphene, rendering it a promising material platform for the elucidation of the mechanism.

For G/Ni, however, much larger Ni hydroxide flakes grow outside the graphene with few confined in the pores (Fig. 1d). This morphology is consistent with those formerly observed for typical metal hydroxides, which have brucite-like structures with hexagonal sheets composed of metal cations. When Fe is introduced, the morphology and hydroxide decoration style become similar to that of G/$NiFe_{0.30}$ (Fig. 1e and f). Interestingly, with the Fe ratio increased, the amount of metal hydroxide nanoparticles rises while the distribution remains uniform, as suggested by the TEM images (Fig. 1b–f) and thermogravimetry analysis (TGA) results (Fig. S2†). The morphology diversity is rationalized by the electrostatic affinity difference between Ni^{2+} and Fe^{3+}. Herein, the CVD-derived graphene was gently oxidized in advance, resulting in a slightly defective and negatively charged surface. Hence, the more positive Fe^{3+} cations exhibited a stronger electrostatic affinity towards the graphene than Ni^{2+} and thereby accelerated the nucleation during the co-precipitation process for a higher decoration density.

The phase and electronic structures of different NiFe hydroxides were investigated using X-ray diffraction (XRD), Fourier transform infrared (FT-IR) spectroscopy, and XPS. As shown in Fig. 2a, G/Ni and G/$NiFe_{0.30}$ share similar diffraction patterns, with the (003) peak representing the intercalation of water and reactive ions in the α-$Ni(OH)_2$ structure (the same as LDH), which has been reported to be the most efficient phase of $Ni(OH)_2$ for OER catalysis.[13] The (012) diffraction peak at 2θ = 33.72° corresponds to a d-space of 0.26 nm, which agrees well with the lattice fringes in the high resolution TEM (HRTEM) image (Fig. S3a and b†), and its asymmetric nature indicates the formation of a turbostratic α-$Ni(OH)_2$ lattice. Meanwhile, in the case of higher Fe content, the XRD patterns are consistent with FeO(OH) rather than with lamellar hydroxide structures (Fig. 2b). The weak intensity and high noise-signal ratio of the G/$NiFe_{0.56}$ and G/Fe diffraction patterns indicates relatively poor crystallization. The hydroxide in the G/Fe sample is assigned to be a polymorph of γ-FeO(OH) and δ-FeO(OH), while the pattern of $NiFe_{0.56}$ suggests successful incorporation of Ni into the FeO(OH) framework to form a $Fe_{0.67}Ni_{0.33}O(OH)$-like structure. A set of lattice fringes with a spacing of 0.25 nm can also been observed in the nanoplates of G/$NiFe_{0.56}$ and G/Fe, which is assigned to the (100) lattice planes (Fig. S3c and d†). Altogether, these results suggest that with the increasing Fe content, the resultant materials are transformed from well-crystallized hydroxides (α-$Ni(OH)_2$ and NiFe LDHs) to amorphous oxyhydroxides (Ni substituted FeO(OH) or an FeO(OH) polymorph, predominantly δ-FeO(OH)) (Fig. S4†), which is believed to be the crucial factor for the corresponding electrocatalytic activities.[31]

The XPS survey scan of the G/NiFe hybrids (Fig. S1, Table S1†) confirms the presence of both Ni and Fe elements in the (oxy)hydroxides and C in the graphene. No distinct spectrum of any Fe species can be identified from the G/Ni sample compared with G/$NiFe_{0.30}$ (Fig. S5a†), which is also supported by the inductively coupled plasma optical emission spectrometry characterization, rationally indicating the α-$Ni(OH)_2$ structure in the G/Ni samples. The high-resolution O 1s spectra of all of the composites reveal three distinct peaks at *ca.* 529.9, 531.3, and 532.4 eV, representing the binding energies of oxygen in C=O or metal–oxide bonds, metal–OH or OH^- bonds, and physi- or chemisorbed water, respectively (Fig. S5b†).[40,41]

In addition, it's notable that the Ni 2p and Fe 2p from the NiFe bimetallic (oxy)hydroxides are both slightly shifted

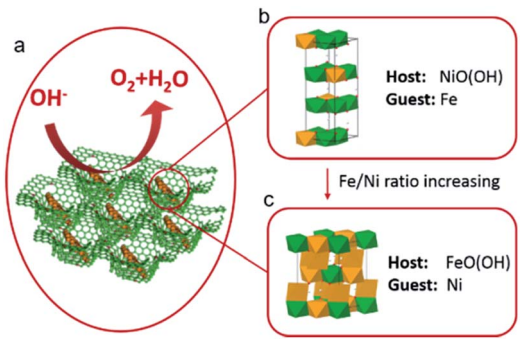

Scheme 1 Schematic diagram of the G/NiFe (oxy)hydroxide composites. (a) Nanosized and ultra-thin NiFe (oxy)hydroxides uniformly decorated on the surface of conductive and mesoporous graphene flakes. (b) Fe doped Ni (oxy)hydroxides at a low Fe content and (c) Ni doped Fe (oxy)hydroxides at a higher Fe content, indicating a phase evolution associated with the Fe/Ni ratio.

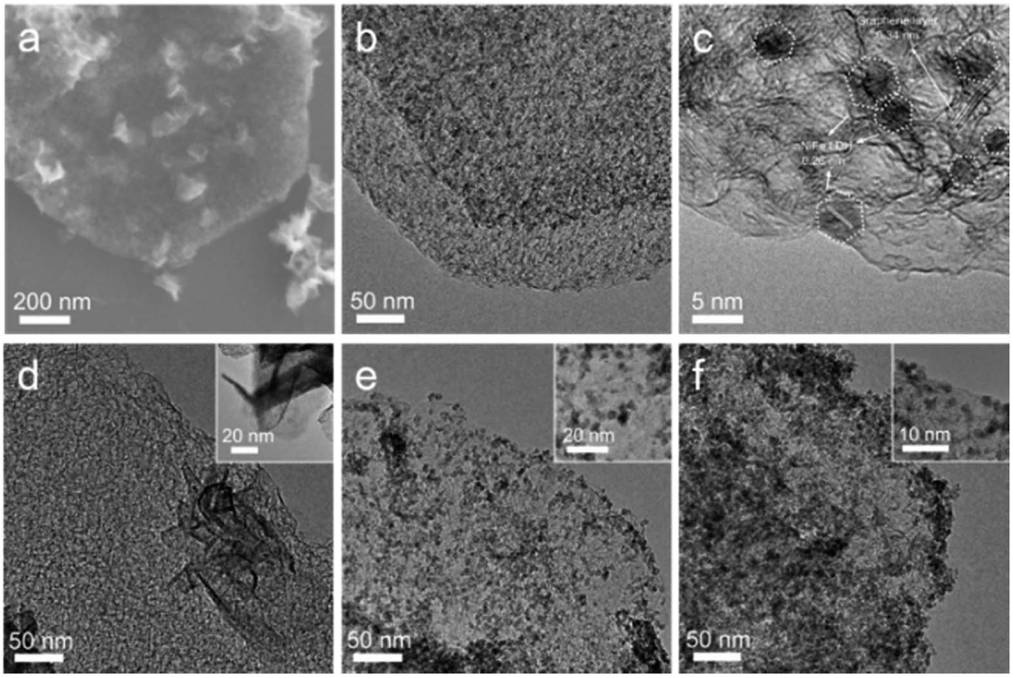

Fig. 1 Morphology of the G/NiFe composites. (a) SEM and (b and c) TEM images of G/$NiFe_{0.30}$, showing a uniform decoration of nanosized NiFe LDHs on graphene. TEM images of (d) G/Ni, (e) G/$NiFe_{0.56}$, (f) G/Fe, indicating different decoration morphologies compared to G/$NiFe_{0.30}$.

compared with the monometallic hydroxides (Fig. 2c and d), indicating a variable electronic environment altered by the Fe/Ni ratio. For G/$NiFe_{0.30}$, Ni $2p_{1/2}$, and Ni $2p_{3/2}$, the peaks are upshifted (~0.9 eV) after the Fe incorporation, while the Fe $2p_{1/2}$ and Fe $2p_{3/2}$ are almost the same. For G/$NiFe_{0.56}$, however, the upshift of the Ni 2p peaks is decreased to ~0.4 eV but with an obvious downshift (~0.4 eV) for the Fe 2p peaks. This difference is believed to be contributed from the guest–host substitution and the bond length variation. For a low Fe content, Fe substitutes into the γ-NiO(OH) lattice and the bond length of Ni–O in the γ-NiO(OH) host is supposed to be expanded; while for a high Fe content, it is Ni substitution into the FeO(OH) framework and the Fe–O length in FeO(OH) host is expected to be contracted, which has been previously demonstrated by Friebel *et al.*[29]

Furthermore, as shown in Fig. 2e, several characteristic FT-IR peaks for hydroxides are generated in addition to the peaks for the oxidized graphene substrate. The peaks around 1380 and 1470 cm^{-1} are assigned to the interlayer CO_3^{2-},[38] and also suggested as the O–H bend of the lattice OH in the metal (oxy) hydroxides.[39] The wide band at about 1630 cm^{-1} is attributed to the O–H bend of layer or free H_2O. The enhanced absorption band at *ca.* 3430 cm^{-1} is ascribed to the O–H stretching vibration of the layer or free H_2O.[39] Notably, a narrow peak appears at 3645 cm^{-1} only for G/Ni and G/$NiFe_{0.30}$ samples, which originates from the O–H stretch of the brucite-like structure.[40] The FT-IR results also support the formation of metal (oxy)hydroxide structures on the graphene substrate.

From the morphological characterization to the physical structure analysis, it is notable to conclude that the Fe/Ni ratio not only tunes the morphology and decoration style in the resultant composites, but also, more importantly, modifies the physical and electronic structures. These diversities arising from the substitution of guest metals into the host (oxy) hydroxide framework contribute to the different properties and performances in OER electrocatalysis.

The OER catalytic activity was measured under alkaline environment (0.10 M KOH), using a standard three-electrode system, with a 0.25 mg cm^{-2} loading of catalyst. At a 5.0 mV s^{-1} scan rate, the typical linear scan voltammogram (LSV) (Fig. 3a) shows that the anodic current densities of all G/NiFe catalysts increase as the potential becomes more positive, which is a common phenomenon in OER catalysis. The peaks at an overpotential of ~250 mV are related to the Ni^{2+}/Ni^{3+} redox reaction. The appropriate incorporation of Fe substantially decreases the onset overpotential from 361 mV for G/Ni to 303 mV for G/$NiFe_{0.30}$ (Table 1). With more Fe substitution, however, the onset overpotential is increased gradually to 430 mV for G/Fe. The overpotentials required to achieve a 10.0 mA cm^{-2} current density, which is a critical OER catalytic parameter, are 567, 372, 390, and 482 mV, for G/Fe, G/$NiFe_{0.30}$, G/$NiFe_{0.56}$, and G/Fe, respectively (Table 1). To assess the durability of different catalysts, a series of chronoamperometric tests were carried out at potentials for an initial OER current density of 1.0 mA cm^{-2} (Fig. 3b). The G/Ni sample shows the best stability with nearly 100% current retention after 8000 s, even at a much higher operation overpotential (360 mV) than G/$NiFe_{0.30}$ (305 mV) or G/$NiFe_{0.56}$ (342 mV). It illustrates the importance of the well-crystallized laminar structure for a better OER stability. The poor stability of G/Fe may be ascribed to the high overpotential (400 mV) required for a similar current density and the amorphous structure. The TEM images and XPS

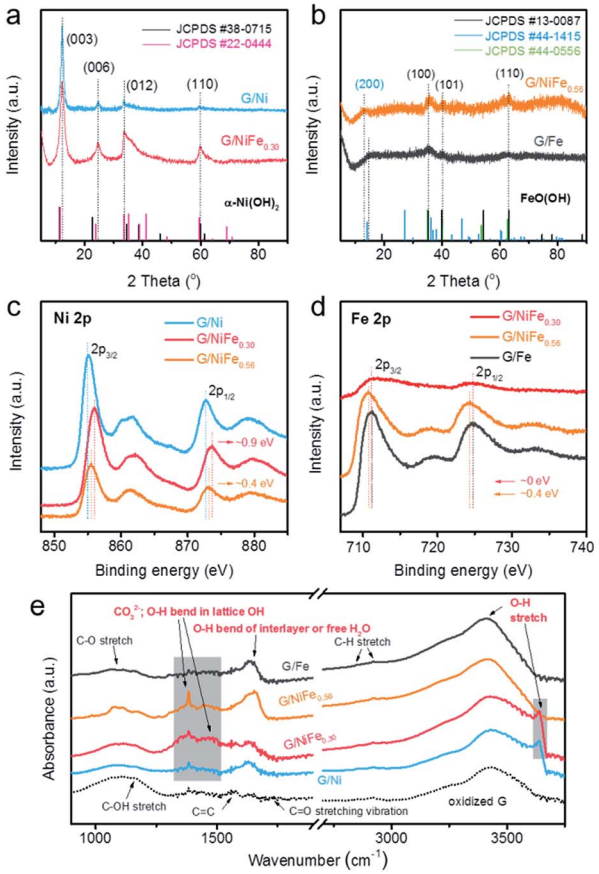

Fig. 2 Structural characterization of the G/NiFe composites. (a) XRD spectra of G/Ni and G/NiFe$_{0.30}$, showing patterns similar to that of α-Ni(OH)$_2$ (JCPDS card no. 38-0715 and 22-0444). (b) XRD spectra of G/Fe and G/NiFe$_{0.56}$, indicating polymorphs of γ-FeO(OH) (JCPDS card no. 44-1415) and δ-FeO(OH) (JCPDS card no. 13-0087), or Fe$_{0.67}$-Ni$_{0.33}$O(OH) (JCPDS card no. 44-0556). (c) High resolution Ni 2p spectra of G/NiFe$_{0.30}$ and G/NiFe$_{0.56}$ compared to G/Ni, with an obvious shift to higher binding energies. (d) High resolution Fe 2p spectra of G/NiFe$_{0.30}$ and G/NiFe$_{0.56}$ compared with G/Fe, with a slight shift to a lower binding energy. (e) FT-IR spectra of the G/NiFe materials and the oxidized graphene substrate.

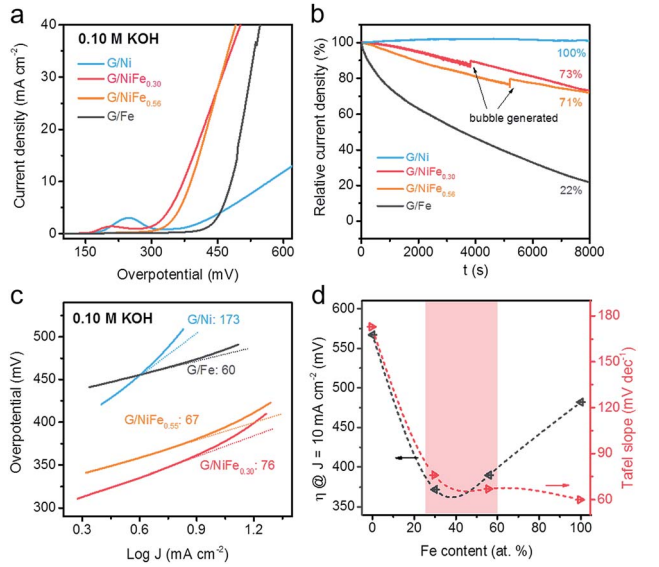

Fig. 3 Oxygen evolution catalysis performances of the G/NiFe composites in 0.10 M KOH electrolyte. (a) LSV curves. Scan rate was 5.0 mV s^{-1}. The loading was about 0.25 mg cm^{-2} for all samples. (b) Chronoamperometric responses for the different samples at a constant potential with an initial current density of 1.0 mA cm^{-2}. (c) Tafel plots of the G/NiFe composites. (d) OER performance as a function of Fe content in consideration of both the activity (overpotential required to achieve 10.0 mA cm^{-2}) and the kinetics (Tafel slope).

spectra of G/NiFe$_{0.30}$ after the 8000 s test indicate the structural stability during OER catalysis (Fig. S6†). Comprehensively, the G/NiFe$_{0.30}$ material exhibits the most promising OER performance, considering the activity and stability.

Meanwhile, the LSV curves of these catalysts exhibit some novel features at higher potentials. For those samples with higher Fe content, the current density rises slowly at first but shows a sharp rise after certain potentials; as indicated by the Tafel plots, G/Fe exhibits the lowest slope of 60 mV dec^{-1}, even lower than that of G/NiFe$_{0.30}$ by 16 mV dec^{-1} (Table 1, Fig. 3b). It is quite interesting that with low Fe content (Fe-substituted NiO(OH)), the overpotential is decreased, while with a higher Fe content (Ni-substituted FeO(OH)), the kinetics is greatly accelerated, but less active until reaching a certain overpotential (Fig. 3c). This should be contributed to the different roles of Ni, Fe, and their oxyhydroxide frameworks, which will be discussed later. The G/NiFe bimetallic (oxy)hydroxide composites have been well-demonstrated to possess an enhanced OER performance over their monometallic counterparts, with an optimized Fe content in the range of 25–60 at%, consistent with other reports.[14,29,34,42]

To elucidate the variation of OER performance in correlation with Fe/Ni ratio, we firstly analyzed the Ni^{2+}/Ni^{3+} redox behaviors for different samples (Fig. 4a). The resultant NiO(OH) phase, oxidized from Ni(OH)$_2$, is believed to be crucial to the activity of NiFe (oxy)hydroxides for OER, whatever the real active sites.[16,29,36] The incorporation of Fe regulates the oxidation state of Ni^{2+}, leading to different redox potentials and current densities.[43] Fig. 4b presents the transferred charge integrated from the redox peak area and corresponding percentage of oxidized Ni^{2+}. The Ni(OH)$_2$/NiO(OH) transformation is demonstrated to be suppressed with increased Fe content. This is consistent with other observations in various NiFe systems[34] and CoFe (oxy)hydroxides as well.[35] If the LSV curves are normalized based on the amount of redox active Ni (resultant Ni^{3+}) in each electrocatalyst, the current density of G/NiFe$_{0.56}$ outperformed that of G/NiFe$_{0.30}$, while still keeping the same onset overpotential trend (inset of Fig. 4b). It is notable that G/NiFe$_{0.56}$ exhibits an oxyhydroxide framework of FeO(OH) rather than NiO(OH) (Fig. 2b). Therefore, this observation can be rationalized by the different intrinsic activities of the host-metal (Ni or Fe) oxyhydroxides and also the distinct modulation effects exerted from the guest-metal (Fe or Ni) substitution.

Besides the active framework and modulation effect, the electrochemically active surface area (ECSA) is another important factor responsible for catalytic activities. The ECSA was

Table 1 OER parameters of the G/NiFe electrocatalysts

Sample	G/Ni	G/NiFe$_{0.30}$	G/NiFe$_{0.56}$	G/Fe
Overpotential for 10.0 mA cm^{-2} (mV)	567	372	390	482
Onset potential – 1.23 V (mV)	361	303	325	430
Tafel slope (mV dec^{-1})	173	76	67	60

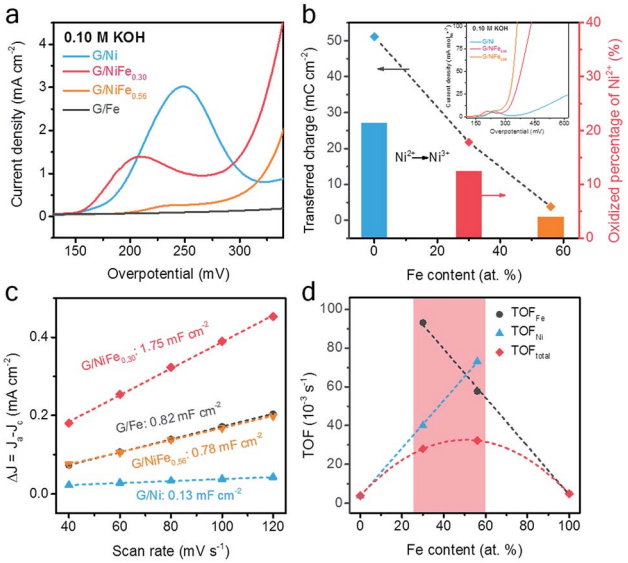

Fig. 4 Elucidation of OER activity *versus* Fe content. (a) Enlargement of the Ni^{2+}/Ni^{3+} redox range in the LSV curves. (b) The charge transferred during the Ni^{2+}/Ni^{3+} transformation and the oxidized percentage from the total Ni^{2+} based on the integral of the redox peak area. The inset LSV curves were normalized based on the amount of redox active Ni (resultant Ni^{3+}) in each material. (c) Charging current density differences plotted *versus* scan rates. The linear slope, equivalent to twice that of the double-layer capacitance C_{dl}, was used to represent the ECSA. (d) TOF depicted based on Fe, Ni, or the total number of Fe and Ni in the working electrodes, correlated with the Fe content.

estimated from the electrochemical double-layer capacitance (C_{dl}) of each electrocatalyst. According to Fig. 4c, G/NiFe$_{0.30}$ possesses the highest ECSA, more than twice that of G/NiFe$_{0.56}$ or G/Fe, which is ascribed to the nanosized lamellar structure and uniform distribution of NiFe oxyhydroxides. The G/Ni sample with its aggregations of much larger $Ni(OH)_2$ flakes delivers the lowest ECSA. As all samples are fabricated under the same condition except for their Fe/Ni ratios, it suggests that the Fe/Ni ratio alters the physical structure and decoration style of the obtained (oxy)hydroxides and results in regulated ECSAs.

To make more eloquent evaluations of the activity variation related to the Fe content, the turnover frequency (TOF) was calculated to compare the intrinsic activities and elucidate their fundamental origin. However, the accurate calculation of TOF is always challenging due to the controversy about the real active sites and also the difficulty of measuring the number of active sites that actually take part in the catalytic process. Here, we systematically calculate TOF values based on the number of Ni and Fe atoms separately or together (denoted as TOF$_{Ni}$, TOF$_{Fe}$, TOF$_{total}$), assuming that only Ni or Fe or both are involved in the catalysis. As plotted in Fig. 4d, both the TOF$_{Ni}$ and TOF$_{Fe}$ increase linearly when the number of assumed active sites decrease. It is ambiguous to conclude whether Ni or Fe atoms are responsible for the real activity sites, as the trends can be ascribed to the net effect rather than intrinsic origin. However, the TOF$_{total}$ of both of the bimetallic (oxy)hydroxides rises almost tenfold compared with their monometallic counterparts, which unequivocally demonstrates the synergistic role of guest and host metals in the multi-metallic (oxy)hydroxides regardless of which one constitutes the host framework.

The observations described here are mostly consistent with other reports;[29,34,35] nevertheless, some new phenomena shed a novel light on the roles of the different components in multi-metallic (oxy)hydroxides. Previous work reports that NiO(OH) serves as the main active substrate in NiFe (oxy)hydroxide OER catalysts, while pure $Ni(OH)_2/NiO(OH)$ itself has little activity,[16] and FeO(OH) is an unstable and inactive framework for OER.[35] The Fe incorporation, even at an ultra-low concentration (0.01%) will activate the next-nearest Ni sites for an enhanced activity,[30,34] or generate new active sites on Fe rather than Ni.[29] With a higher Fe level above the "Fe saturation limit" (25% (ref. 29) or 11% (ref. 36)), a separate and inactive Fe-rich phase (such as a γ-FeO(OH) phase) is supposed to form and decrease the net activity. However, in our research presented here, the Fe doped Ni (oxy)hydroxides and Ni doped Fe (oxy)hydroxides both exhibited superb activities, while distinct in terms of their onset potentials and Tafel slopes, which is quite different from previous reports.

On one hand, the NiO(OH) and FeO(OH) exhibit different physical structures and thereby distinct performances for OER. The metal–OH bond of Fe is longer than Ni with a significantly higher OH affinity. Meanwhile, the lattice Fe–O bond length is shorter than Ni–O, which is associated with different oxidation states.[29] The recent research of the CoFe (oxy)hydroxide system has indicated that FeO(OH) exhibits a higher intrinsic OER activity than CoO(OH), but suffers from poor conductivity and stability.[35] Therefore, a stable and conductive substrate (Ni or Co oxyhydroxide), as well as a high potential are required to demonstrate the intrinsic activity of FeO(OH). In this work, the NiO(OH) phase delivers a lower onset overpotential (361 mV) for a low Fe content, while the FeO(OH) phase increases the current density rapidly (Tafel slope: 60 mV dec^{-1}) after a higher activation overpotential (~440 mV) for a higher Fe content.

On the other hand, the incorporation of Fe into the NiO(OH) lattice (G/NiFe$_{0.30}$) decreases the Tafel slope from 173 to 76 mV dec^{-1}, and the Ni substitution into the FeO(OH) framework (G/NiFe$_{0.56}$) cathodically shifts the onset overpotential by 105 mV but with a slightly increased Tafel slope. This

observation suggests that no matter which one constitutes the host oxyhydroxide framework, the other substitution and modulation will significantly enhance the performance. As the Ni–O sites adsorb all of the OER intermediates too weakly while Fe–O sites too strongly,[29] the wise modulation of NiFe (oxy) hydroxides with an optimal Fe/Ni ratio is believed to alter the metal–oxygen bond length and consequently the intermediate adsorption energy towards optimal values. Remarkably, the G/$NiFe_{0.30}$ exhibits a smaller Tafel slope and onset potential than those of G/Ni, indicating a favorable synergetic effect of the Fe substitution and NiO(OH) framework.

In conclusion, we fabricated a series of G/NiFe (oxy)hydroxides, and investigated the role of the Fe/Ni ratio on the resultant physical structures, decoration styles, and superb OER performance. With the Fe concentration increasing, the as-obtained electrocatalysts evolved from well-crystallized hydroxides (α-$Ni(OH)_2$ and NiFe LDHs) to amorphous oxyhydroxides (Ni substituted FeO(OH) or a FeO(OH) polymorph). Moderate guest-metal substitution into the host oxyhydroxide framework (Fe into Ni or Ni into Fe) substantially enhanced the OER activity with a decrease of both the Tafel slope and overpotential. In addition, both the NiO(OH) and FeO(OH) frameworks exhibited distinct properties and performances for OER due to the different metal–oxygen bonds and adsorption energies. Under the guest incorporation and modulation, both physical and electronic structures are altered, resulting in an optimal metal–oxygen bond length and adsorption sites for OER intermediates. This work provides new insight into the role of the (oxy) hydroxide substrate and guest-metal incorporation for OER catalysis. It is expected to shed fresh light on the rational design of multi-metallic materials for superior electrocatalysis.

Acknowledgements

This work was supported by funding from the Natural Scientific Foundation of China (No. 21306102 and 21422604) and Tsinghua University Initiative Scientific Research Program (2014z22076). We are thankful for the helpful discussion from Ting-Zheng Hou, Jia-Le Shi, Dr Gui-Li Tian, and Dr Xiao-Lin Zhu.

Notes and references

1 S. Chu and A. Majumdar, *Nature*, 2012, **488**, 294–303.
2 I. Katsounaros, S. Cherevko, A. R. Zeradjanin and K. J. J. Mayrhofer, *Angew. Chem., Int. Ed.*, 2014, **53**, 102–121.
3 M. G. Walter, E. L. Warren, J. R. McKone, S. W. Boettcher, Q. X. Mi, E. A. Santori and N. S. Lewis, *Chem. Rev.*, 2010, **110**, 6446–6473.
4 Y. Jiao, Y. Zheng, M. T. Jaroniec and S. Z. Qiao, *Chem. Soc. Rev.*, 2015, **44**, 2060–2086.
5 C. C. L. McCrory, S. Jung, J. C. Peters and T. F. Jaramillo, *J. Am. Chem. Soc.*, 2013, **135**, 16977–16987.
6 M. Gong and H. J. Dai, *Nano Res.*, 2015, **8**, 23–39.
7 J. T. Zhang, Z. H. Zhao, Z. H. Xia and L. M. Dai, *Nat. Nanotechnol.*, 2015, **10**, 444–452.
8 Y. Lee, J. Suntivich, K. J. May, E. E. Perry and Y. Shao-Horn, *J. Phys. Chem. Lett.*, 2012, **3**, 399–404.
9 Y. Yang, H. Fei, G. Ruan, C. Xiang and J. M. Tour, *ACS Nano*, 2014, **8**, 9518–9523.
10 C. Yuan, H. B. Wu, Y. Xie and X. W. Lou, *Angew. Chem., Int. Ed.*, 2014, **53**, 1488–1504.
11 Z. Lu, W. Xu, W. Zhu, Q. Yang, X. Lei, J. Liu, Y. Li, X. Sun and X. Duan, *Chem. Commun.*, 2014, **50**, 6479–6482.
12 L. Cheng, W. J. Huang, Q. F. Gong, C. H. Liu, Z. Liu, Y. G. Li and H. J. Dai, *Angew. Chem., Int. Ed.*, 2014, **53**, 7860.
13 M. Gao, W. Sheng, Z. Zhuang, Q. Fang, S. Gu, J. Jiang and Y. Yan, *J. Am. Chem. Soc.*, 2014, **136**, 7077–7084.
14 M. Gong, Y. Li, H. Wang, Y. Liang, J. Z. Wu, J. Zhou, J. Wang, T. Regier, F. Wei and H. Dai, *J. Am. Chem. Soc.*, 2013, **135**, 8452–8455.
15 F. Song and X. Hu, *J. Am. Chem. Soc.*, 2014, **136**, 16481–16484.
16 L. Trotochaud, S. L. Young, J. K. Ranney and S. W. Boettcher, *J. Am. Chem. Soc.*, 2014, **136**, 6744–6753.
17 G.-L. Tian, M.-Q. Zhao, D. Yu, X.-Y. Kong, J.-Q. Huang, Q. Zhang and F. Wei, *Small*, 2014, **10**, 2251–2259.
18 F. Song and X. Hu, *Nat. Commun.*, 2014, **5**, 4477.
19 M. S. Burke, S. H. Zou, L. J. Enman, J. E. Kellon, C. A. Gabor, E. Pledger and S. W. Boettcher, *J. Phys. Chem. Lett.*, 2015, **6**, 3737–3742.
20 Z. Li, M. Shao, H. An, Z. Wang, S. Xu, M. Wei, D. G. Evans and X. Duan, *Chem. Sci.*, 2015, **6**, 6624–6631.
21 M. Shao, R. Zhang, Z. Li, M. Wei, D. G. Evans and X. Duan, *Chem. Commun.*, 2015, **51**, 15880–15893.
22 Z. Lu, L. Qian, Y. Tian, Y. Li, X. Sun and X. Duan, *Chem. Commun.*, 2016, **52**, 908–911.
23 Y. Li, H. He, W. Fu, C. Mu, X.-Z. Tang, Z. Liu, D. Chi and X. Hu, *Chem. Commun.*, 2016, **52**, 1439–1442.
24 L. J. Zhou, X. X. Huang, H. Chen, P. P. Jin, G. D. Li and X. X. Zou, *Dalton Trans.*, 2015, **44**, 11592–11600.
25 C. Tang, H. S. Wang, H. F. Wang, Q. Zhang, G. L. Tian, J. Q. Nie and F. Wei, *Adv. Mater.*, 2015, **27**, 4516–4522.
26 H. F. Wang, C. Tang and Q. Zhang, *J. Mater. Chem. A*, 2015, **3**, 16183–16189.
27 W. Ma, R. Ma, C. Wang, J. Liang, X. Liu, K. Zhou and T. Sasaki, *ACS Nano*, 2015, **9**, 1977–1984.
28 X. Yu, M. Zhang, W. Yuan and G. Shi, *J. Mater. Chem. A*, 2015, **3**, 6921–6928.
29 D. Friebel, M. W. Louie, M. Bajdich, K. E. Sanwald, Y. Cai, A. M. Wise, M.-J. Cheng, D. Sokaras, T.-C. Weng, R. Alonso-Mori, R. C. Davis, J. R. Bargar, J. K. Norskov, A. Nilsson and A. T. Bell, *J. Am. Chem. Soc.*, 2015, **137**, 1305–1313.
30 D. A. Corrigan, *J. Electrochem. Soc.*, 1987, **134**, 377–384.
31 L. Trotochaud, J. K. Ranney, K. N. Williams and S. W. Boettcher, *J. Am. Chem. Soc.*, 2012, **134**, 17253–17261.
32 D. N. Wang, J. G. Zhou, Y. F. Hu, J. L. Yang, N. Han, Y. G. Li and T. K. Sham, *J. Phys. Chem. C*, 2015, **119**, 19573–19583.
33 O. Diaz-Morales, I. Ledezma-Yanez, M. T. M. Koper and F. Calle-Vallejo, *ACS Catal.*, 2015, **5**, 5380–5387.
34 M. W. Louie and A. T. Bell, *J. Am. Chem. Soc.*, 2013, **135**, 12329–12337.

35 M. S. Burke, M. G. Kast, L. Trotochaud, A. M. Smith and S. W. Boettcher, *J. Am. Chem. Soc.*, 2015, **137**, 3638–3648.
36 S. Klaus, Y. Cai, M. W. Louie, L. Trotochaud and A. T. Bell, *J. Phys. Chem. C*, 2015, **119**, 7243–7254.
37 J. R. Swierk, S. Klaus, L. Trotochaud, A. T. Bell and T. D. Tilley, *J. Phys. Chem. C*, 2015, **119**, 19022–19029.
38 Y. Q. Xu, Y. C. Hao, G. X. Zhang, Z. Y. Lu, S. Han, Y. P. Li and X. M. Sun, *RSC Adv.*, 2015, **5**, 55131–55135.
39 D. S. Hall, D. J. Lockwood, C. Bock and B. R. MacDougall, *Proc. R. Soc. A*, 2015, **471**, 20140792.
40 Y. L. Ge, K. Kan, Y. Yang, L. Zhou, L. Q. Jing, P. K. Shen, L. Li and K. Y. Shi, *J. Mater. Chem. A*, 2014, **2**, 4961–4969.
41 Y. Z. Su, K. Xiao, N. Li, Z. Q. Liu and S. Z. Qiao, *J. Mater. Chem. A*, 2014, **2**, 13845–13853.
42 S. Klaus, M. W. Louie, L. Trotochaud and A. T. Bell, *J. Phys. Chem. C*, 2015, **119**, 18303–18316.
43 L. Trotochaud, S. L. Young, J. K. Ranney and S. W. Boettcher, *J. Am. Chem. Soc.*, 2014, **136**, 6744–6753.